1 **Title:**

2 # Functional channels in mature *E. coli* colonies

3 **Authors:**

4 Liam M. Rooney [1*], William B. Amos [2], Paul A. Hoskisson [1] and Gail McConnell [2]

5 **Author Affiliations:**

6 1. Strathclyde Institute of Pharmacy and Biomedical Sciences, University of Strathclyde, 161
7   Cathedral Street, Glasgow, G4 0RE, United Kingdom
8 2. Department of Physics, SUPA, University of Strathclyde, 107 Rottenrow East, Glasgow,
9   G4 0NG, United Kingdom
10 *Correspondence: liam.rooney@strath.ac.uk

11 **ORCID Identifiers:**

12 Liam M. Rooney – 0000-0002-2237-501X
13 William B. Amos – 0000-0001-9979-5920
14 Paul A. Hoskisson – 0000-0003-4332-1640
15 Gail McConnell – 0000-0002-7213-0686

16 Word count (minus Abstract, Methods, References, Figures & legends): 3001

Abstract

18 Biofilms are important in medicine, industry and the natural environment, however their structure
19 is largely unexplored across multiple spatial scales. We have studied the architecture of mature
20 *Escherichia coli* macro-colony biofilms by means of the Mesolens, an optical system which
21 uniquely allows simultaneous imaging of individual bacteria and over one hundred cubic
22 millimetres of its biofilm milieu. Our chief finding is the presence of intra-colony channels on the
23 order of 10 μm in diameter in *E. coli* biofilms. These channels have a characteristic structure and
24 reform after total mechanical disaggregation of the colony. We present evidence that the channels
25 transport particles and function to assist the absorption of nutrients. These channels potentially
26 offer a new route for the delivery of dispersal agents or antimicrobial drugs to biofilms, ultimately
27 lowering their impact on public health and industry.

Introduction

Though often inconspicuous, biofilms are one of the most prolific and metabolically active environments on Earth. Biofilms are aggregate communities of microbes held together by extracellular matrices containing extracellular polysaccharides (EPS) and nucleic acids[1,2]. These microbial communities can be composed of one or more species (mono/poly-microbial) and are found in almost every ecological niche[3]. The protective matrix enveloping the biofilm confers resistance to desiccation and exposure to diffusing agents such as biocides or antibiotics[4–8], in turn promoting the development and spread of antimicrobial resistance[9]. Consequently, the study of biofilm structure is vital to understanding and combatting the development of resistance and lowering the clinical and industrial burden of biofilms. The 3D organisation of biofilms can take many forms[10–13]; for example, mushroom-shaped biofilms grown in liquid flow systems, thin sheet-like biofilms in static liquid systems, pellicle biofilms grown at liquid/air interfaces, and macro-colony biofilms grown on solid surfaces. Although morphologically distinct, what classifies these structurally-different communities as 'biofilms' lies with their shared fundamental biochemical signals and pathways[3].

Dynamic computational modelling programmes, such as CellModeller[14,15], have been routinely used to predict the spatial patterning and arrangement of cells within bacterial communities[14–18]. *In silico* models primarily show growth of polymicrobial communities where cell shape, size, surface properties and cell-cell interactions influence the spatial organisation of the mature biofilm, resulting in sectoring of different strains into distinct populations, which has been validated experimentally[19–23]. However, *in silico* modelling has shown little evidence of structural ordering or complex spatial patterning, and a lack of effective multi-scale imaging techniques has presented little experimental evidence of 3D structure within mono-strain biofilms.

There has been much imaging of living biofilms. For example, the density-dependent phage sensitivity in *Escherichia coli* colonies has been studied[24], the biofilms present on human tooth enamel have been imaged at different pH levels[25], and synchronies of growth and electrical signalling between adjacent bacterial colonies have been observed[26]. Such studies have exposed a gap in the repertoire of the optical microscope in that either microbes could be individually imaged with a high-power objective lens, or the overall structure could be viewed at low magnification with resolution so poor, particularly in depth, that individual microbial cells could not be seen. To address this, we use the Mesolens to image intact live macro-colony biofilms *in situ* with isotropic sub-cellular resolution. In essence, the Mesolens is a giant objective lens with the unique combination of 4x magnification with a numerical aperture (NA) of 0.47; which is

61 approximately five-times greater than that of a conventional 4x objective lens[27]. The low
62 magnification coupled with a high NA result in a field of view (FOV) measuring approximately 6
63 mm^2 with lateral resolution of 700 nm and 7 μm axially, while the lens prescription provides a
64 working distance of 3 mm. Moreover, the lens is chromatically corrected across the visible
65 spectrum and designed to be compatible with various immersion routines. While the Mesolens
66 has proven to be a powerful tool in neuroscience, developmental biology and pathology[27–29], it
67 also presents an untapped technology for biofilm imaging, where we can image whole live
68 microbial communities with unprecedented detail within a single dataset without additional
69 processing or stitching and tiling.

70 We explored the internal architecture of mature *E. coli* macro-colony biofilms using a novel
71 mesoscopic imaging approach. We identified and characterised a previously undocumented
72 channel system within *E. coli* biofilms. These channels allow for nutrient uptake from the external
73 environment, which offers a novel mechanism for nutrient delivery in microbial communities
74 beyond passive diffusion; which is widely accepted as the main route of delivery for any external
75 compounds to enter a biofilm, whether they be nutrients or antimicrobial drugs[15,16,14,17]. Using
76 fluorescent probes, we determined that intra-colony channels have a significant protein
77 component. Additionally, we demonstrated that intra-colony channels form as an emergent
78 property of biofilm formation in *E. coli*. These findings provide novel understanding of how spatial
79 organisation in bacterial biofilms contributes to their ability to transport material from the external
80 environment – a function which could be exploited to target biofilm dispersal agents and
81 antimicrobial drugs to lower the burden of biofilms on public health.

82 # Results

83 **Identification of a network of intra-colony channels in *E. coli* biofilms**

84 We investigated the internal architecture of *E. coli* macro-colony biofilms using conventional
85 widefield epi-fluorescence microscopy, widefield mesoscopy and confocal laser scanning
86 mesoscopy. Using widefield mesoscopy we discovered that *E. coli* (JM105) biofilms contain a
87 network of channel-like structures which permeate the biofilm and travelled from the centre to the
88 leading edge. The channels measure approximately 15 μm wide and appear as non-fluorescing
89 regions within the biofilm which are lined by individual cells in a pole-to-pole arrangement. We
90 applied a Classic Maximum Likelihood Estimation deconvolution algorithm to a z-stack acquired
91 using the Mesolens in widefield epi-fluorescence mode to improve image quality and reveal the

92   arrangement of individual cells in a mature macro-colony biofilm. We then applied a colour-coded

93   look-up table (LUT) according to the axial position of each optical section within the 36 μm-thick

94   z-stack (Figure 1). From the axial-coded LUT we can see that the intra-colony channels are not

95   merely 2D lateral arrangements of cells, but that the channels have a 3D topography within the

96   context of the biofilm, resembling canyons and ravines rather than enclosed capillaries.

97   Additionally, we imaged JM105 biofilms using confocal mesoscopy to ensure that the

98   deconvolution algorithm that we used when processing widefield Mesolens data did not introduce

99   erroneous structural artefacts. Confocal microscopy provides a marked improvement in signal-to-

100   noise ratio compared to widefield techniques, particularly with thick specimens, resulting in a

101   similar image quality to a deconvolved widefield dataset. Confocal mesoscopy revealed the same

102   channel structures that we identified in widefield imaging experiments presented in Figure 1

103   (Supplementary Figure 2, Supplementary Movie 1). This concludes that the structures we

104   observed were not introduced as an artefact of image processing.

105   To demonstrate the benefit of using the Mesolens over conventional microscopes for imaging live

106   biofilms, we also imaged biofilms using a conventional upright widefield epi-fluorescence

107   microscope with a low-magnification, low-NA lens (4x/0.13 NA). We compared the ability of the

108   Mesolens and the conventional microscope to resolve the intra-colony channels and found that

109   there was a clear improvement in the spatial resolution with the Mesolens (Supplementary Figure

110   3). The resolution improvement applies to both lateral and axial resolution, and establishes the

111   Mesolens as an ideal imaging technology for 3D imaging of large microbiological specimens with

112   sub-micron resolution.

113   **A structural assessment of intra-colony channels**

114   The channel structures we have identified appear as dark regions within the biofilm, and so we

115   hypothesised that they contained some form of structural matrix. We began investigating the

116   structural makeup of the channels by determining if they were filled with materials of differing

117   refractive index compared to that of the biomass. Possible candidates were solid growth medium

118   which was forced upward during biofilm growth, or air which was trapped in the biofilm. We used

119   reflection confocal mesoscopy where signal is detected from reflections of incident light at

120   refractive index boundaries, such as those between bacterial cells and the surrounding growth

121   medium. A maximum intensity projection of an unlabelled *E. coli* JM105 biofilm acquired in

122   reflection confocal mode showed no reflection signal resembling the intra-colony channels which

123   we report (Figure 2a). This informs us that the channels must be of a similar refractive index to

124   the surrounding biomass and biofilm matrix and are not occupied by solid growth medium or air.

125 To determine if the channel structures we observe were occupied by non-viable/non-fluorescing

126 cells, biofilms were grown in the presence of the viability dye, Sytox Green. This dye has an

127 emission peak at 523 nm enabling the use of HcRed1 $(\lambda_{em.}$ 618 nm) expressing JM105 *E. coli*

128 cells for two-colour imaging. Figure 2b shows a false-coloured composite maximum intensity

129 projection of a JM105-miniTn7-*HcRed1* biofilm stained with Sytox Green acquired using widefield

130 mesoscopy, where live cells are presented in cyan and non-viable cells are shown in yellow. We

131 subtracted the signal of the non-viable cells from HcRed1-expressing cells to prevent spectral

132 overlap in the emission of the two fluorophores, meaning that no Sytox-labelled cells were falsely

133 presented in cyan. We observed that viable and non-viable cells formed two distinct domains

134 within the colony. Here, non-viable cells cluster in the centre of the biofilm while intra-colony

135 channels are not occupied by non-viable/non-fluorescent cells.

136 To investigate whether intra-colony channels were filled with exopolysaccharides (EPS) secreted

137 by bacteria within the biofilm, we grew JM105 biofilms in the presence of the lectin binding dye

138 conjugate Alexa594-Wheat germ agglutinin (WGA). Figure 2c shows a deconvolved composite

139 image of a JM105-miniTn7-*gfp* biofilm (green) and associated EPS (magenta).

140 Exopolysaccharides are distributed throughout the entire biofilm and are not strictly localised

141 within the channel structures. We assessed lipid distribution using the lipid-binding dye Nile Red,

142 which showed that intra-colony channels are not composed of a lipid matrix (Figure 2d).

143 Extracellular proteins were stained using the protein-specific fluorescent dye, SYPRO Ruby. The

144 intra-colony channels contained extracellular protein (Figure 2e). The finding that the channels

145 are filled by a protein matrix suggests that they arise not due to some stochastic process and that

146 the channels have some function.

147 **Channels emerge as an inherent property of biofilm formation**

148 To determine whether the formation of intra-colony channels arose as an emergent property of

149 biofilm formation, we investigated if the structures were able to re-form following disruption. We

150 allowed the biofilm to establish the formation of channels (Figure 3a) and then disturbed the

151 colony, by mixing to create a uniform mass of cells. Following a recovery period of 10 hours, the

152 channels reformed in the regrowing regions of the biofilm (Figure 3b). The ability of the channels

153 to form in the same way as a naïve colony suggests that they form as an emergent property of *E.*

154 *coli* colonial growth on a solid surface.

155 **Channels are unable to cross strain boundaries in mixed isogenic cultures**

156 Growth of two isogenic strains in co-culture, each expressing a different photoprotein, two strains
157 formed sectors as has been previously described [18–20,22,21,23]. We wished to explore this sectoring
158 property in the context of intra-colony channel formation and to determine if the channels were
159 shared between the strains. When the two isogenic strains sector, the channels do not intersect
160 the boundary between the strains and are retained within the own sector (Figure 4). The
161 confinement of channels was more evident between different populations (i.e. HcRed1 and GFP-
162 expressing), whereas the boundaries between sectors of cells expressing the same photoprotein
163 were less ordered.

Intra-colony channels present a novel nutrient acquisition system in *E. coli* biofilms

165 To investigate whether the intra-colony channels play a role in the transport of substances into
166 the biofilm, the functional role of the channel system was tested by introducing 200 nm diameter
167 fluorescent microspheres to the extracellular medium when preparing the specimen for widefield
168 mesoscopy. The fluorescent microspheres were spread as a dense lawn along with a dilute mid-
169 log JM105-miniTn7-*gfp* culture. A single optical section, 25 μm above the base of the colony,
170 allows the outline of the colony to be observed at the edges of the image, with the untouched
171 lawn of microspheres outside the colony (Figure 5a). The distribution of beads in these areas are
172 homogenous, whereas within the colony the transport of the fluorescent microspheres through
173 the channels reflects the spatial structure of the biofilm. Magnified regions of interest (ROI) of
174 intra-colony channels show that the channels are acting as conduits for the transport of
175 microspheres into the biofilm (Figure 5b). The transport of microspheres into the channels
176 suggests that these intra-colony structures are involved in the acquisition of substances from the
177 external environment. We suggest the ability of channels to transport small fluorescent particles
178 could be extended to facilitate uptake of smaller particles into the colony, such as nutrients.

179 To further investigate the role of intra-colony channels in biofilm nutrient acquisition, an arabinose
180 inducible GFP strain (*E. coli* JM105 P$_{BAD}$-*gfp*) was used. Growth of the arabinose-inducible GFP
181 strain on solid minimal medium with L-arabinose as the sole carbon source revealed the biofilm
182 fluoresced most intensely in regions which bordered the intra-colony channels (Figure 6). This
183 suggests that the concentration of L-arabinose is highest in the channel system compared to the
184 remainder of the biofilm and demonstrates the role of these structures in nutrient acquisition and
185 transport within the colony. This finding challenges the long-held belief that bacterial colony
186 nutrient uptake occurs through simple diffusion through the extracellular matrix of the biofilm, and
187 concurs with previous work which suggested that large biofilms must develop transport
188 mechanisms to direct nutrients to their centre[1].

Discussion

This study is the first application of the Mesolens to microbiology and has offered a new approach for imaging large microbial specimens, enabling us to characterise a novel structural aspect of *E. coli* macro-colony biofilms. The channel structures reported are formed as an emergent property of biofilm growth and are confined within founder cell boundaries in mixed isogenic cultures. We have also established a functional role for intra-colony channels in nutrient acquisition and transport. The identification and characterisation of these previously undocumented channels offers a novel outlook for microbial community biology and provides a novel mechanism for nutrient delivery in bacterial biofilms.

Previous biofilm imaging studies have mainly used conventional widefield and laser scanning microscopy to study biofilm architecture, which are inherently limited by sacrificing spatial resolution and imaging volume. For example, automated tile-scanning microscopes which change the location of the FOV or focal plane have been used to image growing colonies from 1×10^1-1×10^4 cells[30–32]; however, this method often requires long acquisition periods and results in tiling artefacts. With the Mesolens we negate the need for stitching and tiling when imaging multi-millimetre specimens and can image beyond small bacterial aggregates to visualise live bacterial macro-colonies in excess of 1×10^9 cells while maintaining sub-micron resolution throughout the entire 6 mm^2 field. Therefore, in comparison with other conventional large specimen imaging techniques, the Mesolens stands as a novel and improved method for *in situ* imaging of live bacterial communities. Additionally, recent advances in light sheet microscopy[33] and mutli-photon microscopy[34,35] have been applied to biofilm imaging. However, these methods currently cannot resolve sub-micron information over multi-millimetre scales, as with the Mesolens. The same problem accompanies ultrasound[36,37], optical coherence tomography and photoacoustic tomography[38–40] methods used for mesoscale biofilm imaging, where they cannot properly resolve structures on the order of which we report. We have also studied images of bacterial macro-colonies under a widely available conventional stereomicroscope. Careful comparison with Mesolens images suggests that traces of the channel may be faintly visible in spite of the low resolution of stereomicroscopes in x, y and particularly z-dimensions.

The structures we have identified bear similarities to some other aspects of bacterial community architecture, however it is important to note that the channels we identify are fundamentally different to structures such as the water irrigation channels discovered in mushroom-shaped *Pseudomonas* and *Klebsiella spp*. biofilms[41,42]. There have also been channel-like structures identified in mature bacterial colonies, such as the crenulations of *B. subtilis* macro-colonies[43,44]

222   or the macroscopic folds of *P. aeruginosa* biofilms[45,46], which have been extensively described in

223   literature. It is important to note, that crenulations and folds are all visible as surface structures of

224   the colony and resolvable using photography techniques, whereas the intra-colony channels

225   identified here are present within the main body of the biofilm and are not observable by viewing

226   the surface of the colony. A similar phenomenon was recently reported in colonies of *Proteus*

227   *mirabilis* where 100 nm diameter fluorescent microspheres were observed to penetrate the

228   boundary of the colony through "crack-like conduits" present at the colony edge[55]. However, the

229   authors were unable to show any spatial evidence of the conduits themselves.

230   The spatial arrangement of the intra-colony channels is fractal in nature, with repeating patterns

231   and complex topographies. Upon first glance, channels resemble fractal features found in multi-

232   strain colonies which form as a result of the mechanical instability between growth and viscous

233   drag of dividing cells[19]. However, these features have only been reported in multi-strain colonies

234   where the fractal dendrites have been composed of live, fluorescing cells[20–23,47]. We demonstrate

235   that the spatial patterns we observe are different to those outlined previously. Firstly, the patterns

236   we observe arise in a single population of cells where there are no strain-to-strain interactions to

237   result in the formation of fractal patterns. Given that the intra-colony channels are not occupied

238   by dead non-fluorescing cells (Figure 2b) it is clear that the bacterial colonies used in this work

239   are not composed of two pseudo-domains (i.e. viable and non-viable cells) which could interact

240   to form complex 3D fractal patterning. Our finding that non-viable cells localise in the centre of

241   the biofilm agrees with previous studies showing that dense microbial aggregates often have

242   dense hypoxic, acidic centres which have diminished access to nutrients[11,12,34,48–52].

243   The intra-colony channels form as an inherent property of biofilm formation, leading to fractal-like

244   patterns which exhibit plasticity which is reminiscent of the results of a classical eukaryotic

245   developmental biology experiment by Moscona, where reformation of the channel architecture in

246   marine sponges occurred after disaggregation by passage through a fine silk mesh[53,54]. The ability

247   of the channels to reform also suggests that they fulfil a functional role in the context of the biofilm.

248   In summary, we have identified a previously undocumented nutrient uptake system in colonial

249   biofilms which challenge the current belief that cells which are out with the reach of underlying

250   nutrient-rich medium are able to gain nutrients beyond simple diffusion through the base of the

251   biofilm[14–17]. The presence of these channels may represent a route to circumvent the chemical

252   protection and resistance phenotype of bacterial biofilms[56], such that rather than applying drugs

253   to the apical surface of the biofilm it may be possible to exploit the intra-colony channels for

254   delivery of antimicrobial agents. The identification and characterisation of an intra-colony channel

255 network could therefore have far-reaching applications to public health and disease prevention,

256 while providing another understanding on the delivery of nutrients to the centre of densely packed

257 microbial communities.

Materials and Methods

258

Designing and 3D-printing a chamber slide for biofilm imaging

259

260 A custom imaging chamber was designed using AutoCAD (Autodesk, USA) with the purpose of

261 imaging large-scale cultured bacterial communities *in situ* using the Mesolens. The design

262 consisted of a plate with dimensions 90 mm x 80 mm x 12 mm and a central well measuring 60

263 mm in diameter with a depth of 10 mm (Supplementary Figure 1). The imaging chamber was 3D-

264 printed using black ABS plastic (FlashForge, Hong Kong) with a FlashForge Dreamer 3D printer

265 (FlashForge, Hong Kong). The chamber slide was sterilised prior to use with 70% ethanol and

266 UV irradiation for 15 minutes.

Bacterial strains and growth conditions

267

268 All experiments were performed using the *E. coli* strains outlined in Supplementary Table 1.

269 Colony biofilms were grown by inoculating a lawn of cells at a density of $1x10^4$ cfu/ml on either

270 solid LB medium or M9 minimal medium[57] supplemented with the appropriate selective antibiotic

271 to achieve single colonies. The colonies were grown in the 3D-printed imaging mould at 37°C for

272 18-24 hours in darkened conditions prior to imaging.

Specimen preparation

273

274 For colony imaging alone, colonies were submerged in sterile LB broth (refractive index (n) =

275 1.338) as a mounting medium following the allocated growth time prior to imaging. A large

276 coverglass was placed over the central well of the imaging mould (70 mm x 70 mm, Type 1.5,

277 0107999098 (Marienfeld, Lauda-Koenigshofen, Germany)), and the colonies were then imaged

278 using either the Mesolens or a conventional widefield epi-fluorescence microscope to compare

279 their performance and to justify using the Mesolens to study biofilm architecture over conventional

280 techniques.

281 The refractive index of the LB mounting medium was measured using an Abbe Refractometer

282 (Billingham & Stanley Ltd., U.K.) which was calibrated using Methanol at 21°C.

Conventional widefield epi-fluorescence microscopy

283

Colony biofilms were imaged on a conventional an Eclipse E600 upright widefield epi-fluorescence microscope (Nikon, Japan) equipped with a 4x/0.13 NA PLAN FLUOR objective lens (Nikon, Japan). GFP excitation was provided by a 490 nm LED from a pE-2 illuminator (CoolLED, U.K.), and emission was detected using a bandpass filter (BA 515-555 nm, Nikon, Japan) placed before an ORCA-spark digital CMOS camera (Hamamatsu, Japan). The camera detector was controlled using WinFluor software[58]. Colonies were imaged after 20 hours of growth in an imaging mould as described above.

Widefield epi-fluorescence mesoscopy

Specifications of the Mesolens have been previously reported[27], and therefore only the imaging conditions used in this study will be outlined here. GFP excitation was achieved using a 490 nm LED from a pE-4000 LED illuminator (CoolLED, U.K.). A triple bandpass filter which transmitted light at 470 ± 10 nm, 540 ± 10 nm and 645 ± 50 nm was placed in the detection pathway. The emission signal was detected using a VNP-29MC CCD camera with chip-shifting modality (Vieworks, South Korea) to capture the full FOV of the Mesolens at high resolution. Widefield mesoscopic imaging was carried out using water immersion (n = 1.33) with the Mesolens' correction collars set accordingly to minimise spherical aberration through refractive index mismatch.

Confocal laser scanning mesoscopy

For laser scanning confocal mesoscopy specimens were prepared as outlined above. Fluorescence excitation of GFP was obtained using the 488 nm line set at 5 mW from a multi-line LightHUB-4 laser combiner (Omicron Laserage, Germany). The green emission signal was detected using a PMT (P30-01, Senstech, U.K.) with a 550 nm dichroic mirror (DMLP550R, Thorlabs, USA) placed in the emission path and a 525/39 nm bandpass filter (MF525-39, Thorlabs, USA) placed before the detector.

For reflection confocal mesoscopy incident light was sourced from a 488 nm line set at 1 mW from a multi-line LightHUB-4 laser combiner (Omicron Laserage, Germany). Reflected signal was detected using a PMT (P30-01, Senstech, U.K.) with no source-blocking filter in place.

Confocal laser scanning mesoscopy was carried out using type DF oil immersion (n = 1.51) with the Mesolens' correction collars set accordingly to minimise spherical aberration through refractive index mismatch.

Structural assessment of intra-colony channels

315   To characterise the structure of intra-colony channels we sought to visualise the distribution of

316   several archetypal structural components of biofilms.

317   As the biofilms in this study were submerged during imaging in a medium with known refractive

318   index, we were able to determine if channels were filled with substances of differing refractive

319   index (e.g. air) using reflection confocal mesoscopy as above. Solid LB was cast into a 3D printed

320   imaging chamber and inoculated with JM105 at a density of $1x10^4$ cfu/ml and incubated for 18-24

321   hours at 37°C in darkened conditions. Biofilms were mounted in sterile LB medium (n = 1.338)

322   prior to imaging.

323   We then imaged the distribution of non-viable cells in the biofilm based on the approach

324   developed by Asally[43]. Briefly, JM105-miniTn7-*HcRed1* colony biofilms were grown for imaging in

325   3D-printed imaging moulds as outlined previously. LB medium was supplemented with gentamicin

326   (20 μg/ml) and 0.5 μM Sytox green dead-cell stain (S7020, Invitrogen, USA). Cells were seeded

327   at a density of $1x10^4$ cfu/ml and grown for 18-24 hours prior to imaging on the Mesolens in

328   widefield epi-fluorescence mode as described above. A 490 nm and a 580 nm LED from a pE-

329   4000 LED illuminator (CoolLED, U.K.) were used to excite Sytox Green and HcRed1 respectively.

330   The emission signal was detected using a VNP-29MC CCD detector (Vieworks, South Korea)

331   with 3x3 pixel-shift modality enabled and with a triple band pass filter (470 ± 10 nm, 540 ± 10 nm

332   and 645 ± 50 nm) in the emission path.

333   To visualise the distribution of EPS in the biofilm we stained sialic acid and *N*-acetylglucosaminyl

334   residues by supplementing solid M9 medium (0.2% glucose (w/v))[57] with 20 μg/ml gentamicin and

335   2 μg/ml Alexa594-WGA (W11262, Invitrogen, USA) before inoculating with $1x10^4$ cfu/ml JM105-

336   miniTn7-*gfp* and growing as previously described. We imaged EPS-stained specimens using

337   widefield epi-fluorescence mesoscopy as before using a 490 nm LED to excite GFP and 580 nm

338   LED to excite Alexa594-WGA.

339   We determined the lipid localisation throughout the biofilm by staining with Nile Red. We

340   supplemented solid LB medium with 20 μg/ml gentamicin and 10 μg/ml Nile Red (72485, Sigma-

341   Aldrich, USA) before inoculating with $1x10^4$ cfu/ml JM105-miniTn7-*gfp* and growing as previously

342   described. We then imaged the lipid distribution in relation to the intra-colony channels using

343   widefield epi-fluorescence mesoscopy as before using a 490 nm LED to excite GFP and 580 nm

344   LED to excite Nile Red.

345   The protein distribution was determined by staining the biofilm with FilmTracer SYPRO Ruby
346   biofilm matrix stain (F10318, Fisher Scientific, USA) which binds to a number of different classes
347   of extracellular protein. Solid LB medium was prepared containing 20 μg/ml gentamicin and a final
348   concentration of 2% (v/v) FilmTracer SYPRO Ruby biofilm matrix stain before inoculating with
349   JM105-miniTn7-*gfp* and growing as previously described. Specimens were imaged using
350   widefield epi-fluorescence mesoscopy. A 490 nm and a 580 nm LED from a pE-4000 illuminator
351   (CoolLED, UK) were used for GFP and SYPRO Ruby excitation, respectively. Fluorescence
352   emission from GFP and SYPRO Ruby were detected as outlined above. Both channels were
353   acquired sequentially.

Disruption and recovery of intra-colony channel structures

355   To assess the ability of the structures we observe to recover following disruption, single colonies
356   of JM105-miniTn7-*gfp* were grown on solid LB medium supplemented with 20 μg/ml gentamicin
357   and allowed to grow for 10 hours at 37°C in darkened conditions. Following the initial growth step
358   colonies were removed from the incubator and gently mixed with a sterile 10 μl pipette tip to
359   disrupt the channel structures in the growing biofilm. Care was taken to prevent disruption to the
360   underlying solid medium on which the colony was supported. Following disaggregation, the
361   colonies were grown for a further 10 hours at 37°C in darkened conditions prior to imaging.
362   Colonies were then mounted in sterile LB medium and imaged using widefield epi-fluorescence
363   mesoscopy as described above.

Using differentially labelled isogenic strains to observe channels in mixed cultures

365   The phenomenon of strain sectoring has been previously documented and occurs by mechanical
366   buckling as adjacent colonies expand into each other during radial growth[18,19]. We investigated
367   whether intra-colony channels were able to cross the strain boundary between sectors by
368   inoculating a low-density mixed culture of JM105-miniTn7-*gfp* and JM105-miniTn7-*HcRed1* at a
369   1:1 ratio and inoculating a lawn onto solid LB medium containing 20 μg/ml gentamicin. We allowed
370   colonies of each strain to stochastically collide into adjacent clonal populations during colony
371   expansion and then imaged using widefield mesoscopy after incubation for 20 hours at 37°C in
372   darkened conditions as described above. We used colony PCR to confirm that the miniTn7
373   insertion, which contained the photoprotein gene, occurred at the same chromosomal location in
374   both strains (*glmS* Fwd. – 5' AAC CTG GCA AAT CGG TTA C; *tn7*R109 Rev. – 5' CAG CAT AAC
375   TGG ACT GAT TTC AG). The miniTn7 transposon inserts at only one *attTn7* site in the
376   chromosome, downstream of *glmS*[59]. We found that both JM105-miniTn7-*gfp* and JM105-

377   miniTn7-*HcRed1* were both inserted approximately 25 base pairs downstream of *glmS*.

378   Therefore, there is no genotypic difference between the strains, save for the inserted photoprotein

379   gene.

Fluorescent microsphere uptake assay

381   To assess the function of the structures we observe, a confluent lawn of fluorescent microspheres

382   was seeded along with the bacterial inoculum at the culturing stage. Two-hundred nanometre

383   multi-excitatory microspheres (Polysciences, Inc., USA) were seeded at a density of 1×10^{10}

384   microspheres/ml and plated along with 1×10^{4} cfu/ml JM105-miniTn7-*gfp* in a mixed-inoculum.

385   Microsphere translocation was assessed by widefield epi-fluorescence mesoscopy as above with

386   two-channel detection for both the GFP and microsphere fluorescence emission. A triple

387   bandpass emission filter which transmitted light at 470 ± 10 nm, 540 ± 10 nm and 645 ± 50 nm

388   was place in the detection path. Sequential excitation of GFP and the fluorescent microspheres

389   was achieved using a 490 nm and 580 nm LED, respectively, from a pE-4000 LED illuminator

390   (CoolLED, U.K.) Each channel was acquired sequentially using a CCD camera detector (Stemmer

391   Imaging, U.K.). All imaging was carried out using water immersion.

Assessing the role of intra-colony channels in nutrient uptake

393   The functional role of the structures which we observe was tested using an arabinose biosensor

394   where GFP expression was controlled by the presence or absence of L-arabinose. The biosensor

395   strain contained the *araBAD* operon with *gfp* inserted downstream on the promotor and ara*BAD*

396   functional genes. The biosensor strain was a gift from colleagues at the James Hutton Institute.

397   JM105 transformed with the arabinose biosensor plasmid, pJM058, were grown overnight at 37°C

398   while shaking at 250 rpm in liquid LB medium supplemented with 25 μg/ml chloramphenicol.

399   Overnight cultures were then diluted in fresh LB and grown until $OD_{600} = 0.5$. Cells were then

400   pelleted and washed three times with 1x M9 salts. Washed cells were inoculated on to solid M9

401   minimal medium[57] with L-arabinose as the sole carbon source (0.2%) at a density of 1×10^{4} cfu/ml

402   and grown for 42-48 hours in darkened conditions at 37°C. Specimens were then prepared for

403   imaging as outlined above.

Image processing and analysis

405   Widefield epi-fluorescence mesoscopy *z*-stacks were deconvolved where specified using with

406   Huygens Professional version 19.04 (Scientific Volume Imaging, The Netherlands, http://svi.nl)

407   using a Classic Maximum Likelihood Estimation algorithm. A theoretical point spread function was

408 generated using Huygens Professional with parameters adjusted to suit the experimental setup.

409 Deconvolution was performed using a server with a 64-bit Windows Server 2016 Standard

410 operating system (v.1607), two Intel® Xeon® Silver 4114 CPU processors at 2.20 GHz and 2.19

411 GHz and 1.0 TB installed RAM. Image analysis was performed using FIJI[60]. Figures presented

412 here were linearly contrast adjusted for presentation purposes where required using FIJI[60].

Acknowledgements

Author Contributions

422 LMR conducted all experiments and analysed all data. LMR, WBA, PAH and GM were

423 responsible for the experimental design. LMR, WBA, PAH and GM prepared the manuscript.

Competing Interests

425 The authors declare no competing interests.

Materials and Correspondence

427 Any requests for materials or correspondence should be directed to LMR.

References

429 1. Hobley, L., Harkins, C., MacPhee, C. E. & Stanley-Wall, N. R. Giving structure to the biofilm matrix:
430   an overview of individual strategies and emerging common themes. *FEMS Microbiol. Rev.* **39**, 649–
431   669 (2015).

432 2. Nadell, C. D., Drescher, K. & Foster, K. R. Spatial structure, cooperation and competition in biofilms.
433   *Nat. Rev. Microbiol.* **14**, 589 (2016).

434 3. Flemming, H.-C. & Wuertz, S. Bacteria and archaea on Earth and their abundance in biofilms. *Nat.*
435 *Rev. Microbiol.* **17**, 247–260 (2019).

436 4. Costerton, J. W. *et al.* Bacterial biofilms in nature and disease. *Annu. Rev. Microbiol.* **41**, 435–64
437 (1987).

438 5. Bixler, G. D. & Bhushan, B. Biofouling: lessons from nature. *Philos. Trans. R. Soc. Math. Phys. Eng.*
439 *Sci.* **370**, 2381–2417 (2012).

440 6. Chaves Simões, L. & Simões, M. Biofilms in drinking water: problems and solutions. *RSC Adv* **3**,
441 2520–2533 (2013).

442 7. Percival, S. L., Suleman, L., Vuotto, C. & Donelli, G. Healthcare-associated infections, medical
443 devices and biofilms: risk, tolerance and control. *J. Med. Microbiol.* **64**, 323–334 (2015).

444 8. Roberts, A. E. L., Kragh, K. N., Bjarnsholt, T. & Diggle, S. P. The Limitations of In Vitro
445 Experimentation in Understanding Biofilms and Chronic Infection. *J. Mol. Biol.* **427**, 3646–3661
446 (2015).

447 9. Carvalho, G., Balestrino, D., Forestier, C. & Mathias, J.-D. How do environment-dependent switching
448 rates between susceptible and persister cells affect the dynamics of biofilms faced with antibiotics?
449 *Npj Biofilms Microbiomes* **4**, (2018).

450 10. Costerton, J. Introduction to biofilm. *Int. J. Antimicrob. Agents* **11**, 217–221 (1999).

451 11. Serra, D. O., Richter, A. M., Klauck, G., Mika, F. & Hengge, R. Microanatomy at Cellular Resolution
452 and Spatial Order of Physiological Differentiation in a Bacterial Biofilm. *mBio* **4**, e00103-13-e00103-
453 13 (2013).

454 12. Ghanbari, A. *et al.* Inoculation density and nutrient level determine the formation of mushroom-
455 shaped structures in <i>Pseudomonas aeruginosa<i> biofilms. *Sci. Rep.* **6**, (2016).

456 13. Sheraton, M. V. *et al.* Mesoscopic Energy Minimization Drives *Pseudomonas aeruginosa* Biofilm
457 Morphologies and Consequent Stratification of Antibiotic Activity Based on Cell Metabolism.
458 *Antimicrob. Agents Chemother.* **62**, (2018).

459 14. Libicki, S. B., Salmon, P. M. & Robertson, C. R. The effective diffusive permeability of a nonreacting
460 solute in microbial cell aggregates. *Biotechnol. Bioeng.* **32**, 68–85 (1988).

461 15. Hunt, S. M., Werner, E. M., Huang, B., Hamilton, M. A. & Stewart, P. S. Hypothesis for the Role of
462 Nutrient Starvation in Biofilm Detachment. *Appl. Environ. Microbiol.* **70**, 7418–7425 (2004).

463 16. Stewart, P. S. Diffusion in Biofilms. *J. Bacteriol.* **185**, 1485–1491 (2003).

464 17. Guélon, T., Mathias, J.-D. & Deffuant, G. Influence of spatial structure on effective nutrient diffusion in
465 bacterial biofilms. *J. Biol. Phys.* **38**, 573–588 (2012).

466 18. Rudge, T. J., Steiner, P. J., Phillips, A. & Haseloff, J. Computational Modeling of Synthetic Microbial
467 Biofilms. *ACS Synth. Biol.* **1**, 345–352 (2012).

468 19. Rudge, T. J., Federici, F., Steiner, P. J., Kan, A. & Haseloff, J. Cell Polarity-Driven Instability
469 Generates Self-Organized, Fractal Patterning of Cell Layers. *ACS Synth. Biol.* **2**, 705–714 (2013).

470 20. Blanchard, A. E. & Lu, T. Bacterial social interactions drive the emergence of differential spatial
471 colony structures. *BMC Syst. Biol.* **9**, (2015).

472 21. Smith, W. P. J. *et al.* Cell morphology drives spatial patterning in microbial communities. *Proc. Natl.*
473 *Acad. Sci.* **114**, E280–E286 (2017).

474 22. Goldschmidt, F., Regoes, R. R. & Johnson, D. R. Successive range expansion promotes diversity
475 and accelerates evolution in spatially structured microbial populations. *ISME J.* **11**, 2112 (2017).

476 23. Jauffred, L., Vejborg, R. M., Korolev, K. S., Brown, S. & Oddershede, L. B. Chirality in microbial
477 biofilms is mediated by close interactions between the cell surface and the substratum. *ISME J.* **11**,
478 1688 (2017).

479 24. Eriksen, R. S., Svenningsen, S. L., Sneppen, K. & Mitarai, N. A growing microcolony can survive and
480   support persistent propagation of virulent phages. *Proc. Natl. Acad. Sci.* **115**, 337–342 (2018).

481 25. Xiao, J. *et al.* Biofilm three-dimensional architecture influences in situ pH distribution pattern on the
482   human enamel surface. *Int. J. Oral Sci.* **9**, 74–79.

483 26. Liu, J. *et al.* Coupling between distant biofilms and emergence of nutrient time-sharing. *Science* **356**,
484   638–642 (2017).

485 27. McConnell, G. *et al.* A novel optical microscope for imaging large embryos and tissue volumes with
486   sub-cellular resolution throughout. *eLife* **5**, e18659 (2016).

487 28. McConnell, G. & Amos, W. B. Application of the Mesolens for subcellular resolution imaging of intact
488   larval and whole adult *Drosophila*. *J. Microsc.* **270**, 252–258 (2018).

489 29. Schniete, J. *et al.* Fast Optical Sectioning for Widefield Fluorescence Mesoscopy with the Mesolens
490   based on HiLo Microscopy. *Sci. Rep.* **8**, (2018).

491 30. Drescher, K. *et al.* Architectural transitions in *Vibrio cholerae* biofilms at single-cell resolution. *Proc.*
492   *Natl. Acad. Sci.* **113**, E2066–E2072 (2016).

493 31. Yan, J., Sharo, A. G., Stone, H. A., Wingreen, N. S. & Bassler, B. L. *Vibrio cholerae* biofilm growth
494   program and architecture revealed by single-cell live imaging. *Proc. Natl. Acad. Sci.* **113**, E5337–
495   E5343 (2016).

496 32. Hartmann, R. *et al.* Emergence of three-dimensional order and structure in growing biofilms. *Nat.*
497   *Phys.* **15**, 251–256 (2019).

498 33. Lagree, K., Desai, J. V., Finkel, J. S. & Lanni, F. Microscopy of fungal biofilms. *Curr. Opin. Microbiol.*
499   **43**, 100–107 (2018).

500 34. Xiao, J. *et al.* Biofilm three-dimensional architecture influences in situ pH distribution pattern on the
501   human enamel surface. *Int. J. Oral Sci.* **9**, 74–79 (2017).

502 35. Thomsen, H. *et al.* Delivery of cyclodextrin polymers to bacterial biofilms — An exploratory study
503   using rhodamine labelled cyclodextrins and multiphoton microscopy. *Int. J. Pharm.* **531**, 650–657
504   (2017).

505 36. Shemesh, H. *et al.* High frequency ultrasound imaging of a single-species biofilm. *J. Dent.* **35**, 673–
506   678 (2007).

507 37. Vaidya, K., Osgood, R., Ren, D., Pichichero, M. E. & Helguera, M. Ultrasound Imaging and
508   Characterization of Biofilms Based on Wavelet De-noised Radiofrequency Data. *Ultrasound Med.*
509   *Biol.* **40**, 583–595 (2014).

510 38. Xi, C., Marks, D., Schlachter, S., Luo, W. & Boppart, S. A. High-resolution three-dimensional imaging
511   of biofilm development using optical coherence tomography. *J. Biomed. Opt.* **11**, 034001 (2006).

512 39. Wagner, M., Taherzadeh, D., Haisch, C. & Horn, H. Investigation of the mesoscale structure and
513   volumetric features of biofilms using optical coherence tomography. *Biotechnol. Bioeng.* **107**, 844–
514   853 (2010).

515 40. Leite de Andrade, M. C. *et al.* A new approach by optical coherence tomography for elucidating
516   biofilm formation by emergent Candida species. *PLOS ONE* **12**, e0188020 (2017).

517 41. Drury, W. J., Characklis, W. G. & Stewart, P. S. Interactions of 1 μm latex particles with
518   <i>Pseudomonas aeruginosa<i> biofilms. *Water Res.* **27**, 1119–1126 (1993).

519 42. Stoodley, P., Lewandowski, Z. & others. Liquid flow in biofilm systems. *Appl. Environ. Microbiol.* **60**,
520   2711–2716 (1994).

521 43. Asally, M. *et al.* Localized cell death focuses mechanical forces during 3D patterning in a biofilm.
522   *Proc. Natl. Acad. Sci.* **109**, 18891–18896 (2012).

523 44. Wilking, J. N. *et al.* Liquid transport facilitated by channels in <i>Bacillus subtilis<i> biofilms. *Proc.*
524   *Natl. Acad. Sci.* **110**, 848–852 (2013).

525 45. Kempes, C. P., Okegbe, C., Mears-Clarke, Z., Follows, M. J. & Dietrich, L. E. P. Morphological
526   optimization for access to dual oxidants in biofilms. *Proc. Natl. Acad. Sci.* **111**, 208–213 (2014).

527 46. Jo, J., Cortez, K. L., Cornell, W. C., Price-Whelan, A. & Dietrich, L. E. An orphan cbb3-type
528   cytochrome oxidase subunit supports Pseudomonas aeruginosa biofilm growth and virulence. 30
529   (2017).

530 47. Nuñez, I. N. *et al.* Artificial Symmetry-Breaking for Morphogenetic Engineering Bacterial Colonies.
531   *ACS Synth. Biol.* **6**, 256–265 (2017).

532 48. Wimpenny, J. W. T. & Coombs, J. P. Penetration of oxygen into bacterial colonies. *Microbiology* **129**,
533   1239–1242 (1983).

534 49. Peters, A. C., Wimpenny, J. W. T. & Coombs, J. P. Oxygen Profiles in, and in the Agar Beneath,
535   Colonies of <i>Bacillus cereus<i>, <i>Staphylococcus albus<i> and <i>Escherichia coli<i>. *J. Gen.*
536   *Microbiol.* **133**, 1257–1263 (1987).

537 50. Jeanson, S., Floury, J., Gagnaire, V., Lortal, S. & Thierry, A. Bacterial Colonies in Solid Media and
538   Foods: A Review on Their Growth and Interactions with the Micro-Environment. *Front. Microbiol.* **6**,
539   (2015).

540 51. Hwang, G. *et al.* Simultaneous spatiotemporal mapping of in situ pH and bacterial activity within an
541   intact 3D microcolony structure. *Sci. Rep.* **6**, (2016).

542 52. Webb, J. S. *et al.* Cell Death in <i>Pseudomonas aeruginosa<i> Biofilm Development. *J. Bacteriol.*
543   **185**, 4585–4592 (2003).

544 53. Moscona, A. A. Aggregation of sponge cells: Cell-linking macromolecules and their role in the
545   formation of multicellular systems. *In Vitro* **3**, 13–21 (1967).

546 54. Lavrov, A. I. & Kosevich, I. A. Sponge cell reaggregation: Mechanisms and dynamics of the process.
547   *Russ. J. Dev. Biol.* **45**, 205–223 (2014).

548 55. Xu, H., Dauparas, J., Das, D., Lauga, E. & Wu, Y. Self-organization of swimmers drives long-range
549   fluid transport in bacterial colonies. *Nat. Commun.* **10**, (2019).

550 56. Jolivet-Gougeon, A. & Bonnaure-Mallet, M. Biofilms as a mechanism of bacterial resistance. *Drug*
551   *Discov. Today Technol.* **11**, 49–56 (2014).

552 57. Elbing, K. L. & Brent, R. Recipes and Tools for Culture of *Escherichia coli*. *Curr. Protoc. Mol. Biol.*
553   **125**, e83 (2019).

554 58. Dempster, J., Wokosin, D. L., McCloskey, K. D., Girkin, J. M. & Gurney, A. M. WinFluor: an
555   integrated system for the simultaneous recording of cell fluorescence images and
556   electrophysiological signals on a single computer system. *Br. J. Pharmacol.* **137**, 146 (2002).

557 59. Lambertsen, L., Sternberg, C. & Molin, S. Mini-Tn7 transposons for site-specific tagging of bacteria
558   with fluorescent proteins. *Environ. Microbiol.* **6**, 726–732 (2004).

559 60. Schindelin, J. *et al.* Fiji: an open-source platform for biological-image analysis. *Nat. Methods* **9**, 676–
560   682 (2012).

561

Figure Legends

Figure 1. **Visualising the intra-colony channel system of *E. coli* macro-colony biofilms.** A deconvolved 36 μm-thick transverse sub-stack of a mature *E. coli* macro-colony biofilm acquired using widefield mesoscopy. An axial colour-coded LUT has been applied which indicates the relative position of each cell within the context of the biofilm. A magnified ROI is presented where individual cells can be clearly resolved. Channel structures are seen to permeate throughout the biofilm and present a 3D topography within the context of the biofilm.

Figure 2. **Characterising the structure of intra-colony channels. (a)** Maximum intensity projection of an unlabelled JM105 colony acquired using reflection confocal mesoscopy, with a single isolated optical section shown. Reflection imaging determined that intra-colony channels were not occupied by material of differing refractive index to the biomass. The colony-medium interface can be observed clearly, while there is no evident structure within the colony. **(b)**. Signal from non-viable cells (yellow) was subtracted from viable cells to negate any spectral overlap in the emission of Sytox Green and HcRed1. A composite maximum intensity projection of the entire colony is presented. Intra-colony channels in the viable cell population (cyan) did not contain any non-viable cells. **(c)** Alexa594-WGA-stained EPS residues (magenta) were not present in the intra-colony channels when compared with elsewhere in the biofilm, meaning channels were not composed of an EPS-based matrix. **(d)** Nile Red-stained lipids (red) clustered in the centre of *E. coli* biofilms while intra-colony channels remain unstained by Nile Red. Therefore, intra-colony channels were not composed of lipids. **(e)** Emission of SYPRO Ruby-stained extracellular proteins (magenta) mimicked the spatial patterns of intra-colony channels, showing that channels were filled by a protein-based matrix.

Figure 3. **Intra-colony channels form as an emergent property of biofilm formation. (a)** An unmixed, naïve control biofilm of JM105-miniTn7-*gfp* with established intra-colony channels. **(b)** A macro-colony JM105-miniTn7-*gfp* biofilm which was initially grown for 10 hours before mechanical disruption and subsequent recovery and regrowth at 37°C for a further 10 hours. Regrowth was accompanied with the re-emergence of intra-colony channels in the outgrown region of the disrupted colony, showing that channel formation is an emergent property of macro-colony biofilm development.
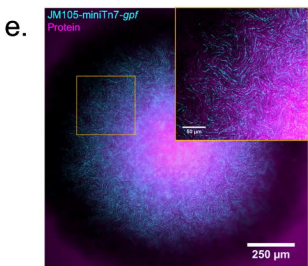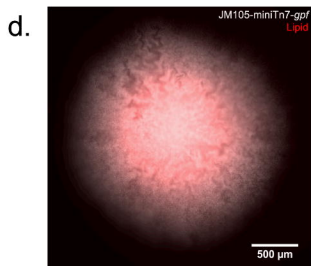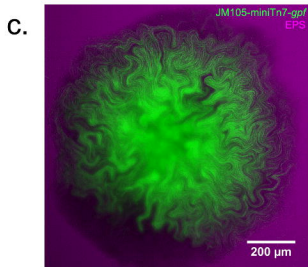
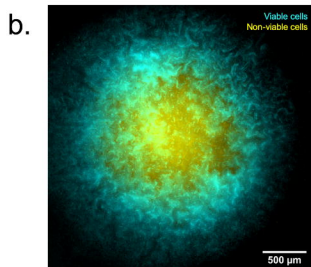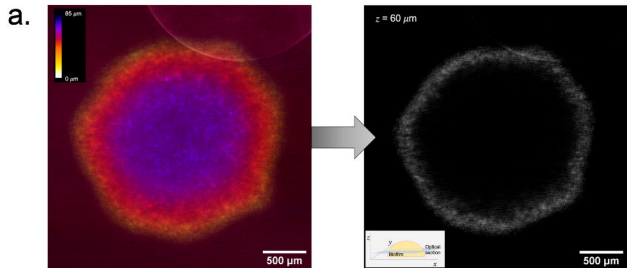Figure 4. **Intra-colony channels are confined within clonal populations and unable to cross strain boundaries**. A mixed culture of isogenic JM105 strains which express either GFP (cyan)
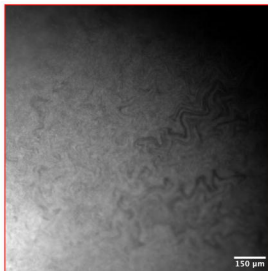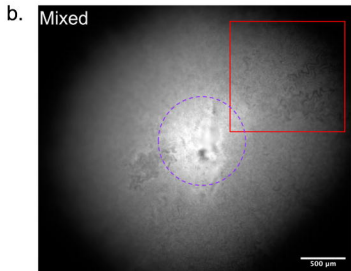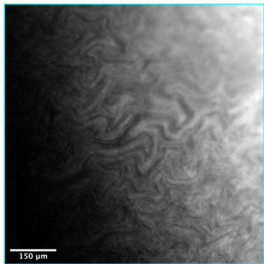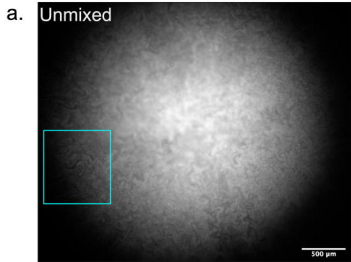
593   or HcRed1 (magenta). Each strain sectored into segregated clonal populations which have

594   propagated from a single colony forming unit, and cells from each sector were unable to cross

595   the strain boundary. The intra-colony channels present within each sector were also unable to

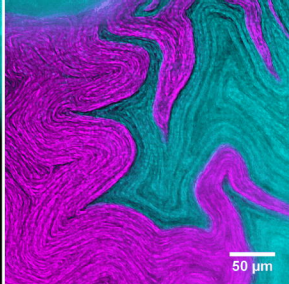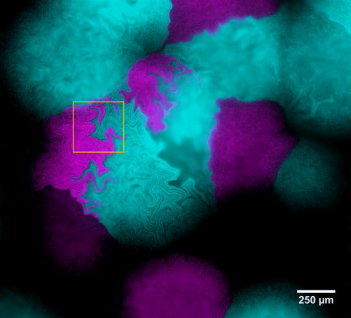596   cross the strain boundary and were therefore not shared by opposing isogenic colonies.

597   Figure 5. **Intra-colony channels facilitate transport of microscopic particles**. A single optical

598   section approximately 25 μm above the base of the colony shows a mature JM105-miniTn7-*gfp*

599   biofilm (green) and a lawn of 200 nm fluorescent microspheres (magenta). The fluorescent

600   microspheres were transported from a confluent lawn at the base of the colony into the intra-

601   colony channels and directed towards the centre of the colony. Two ROIs are presented from

602   different regions of the colony where fluorescent microspheres were transported into the colony

603   via intra-colony channels.

604   Figure 6. **Intra-colony channels play a functional role in nutrient acquisition and transport**

605   **to the centre of bacterial biofilms**. A deconvolved image of a JM105-pJM058 macro-colony

606   biofilm grown on M9 minimal medium with L-arabinose as the sole carbon source. This arabinose

607   biosensor expresses GFP only in the presence of L-arabinose. GFP emission intensity was higher

608   in cells which line the intra-colony channels compared to cells elsewhere within the biofilm, which

609   shows that the channel structures have a higher concentration of L-arabinose compared to

610   elsewhere within the biofilm. This provides evidence of a functional role in nutrient acquisition and

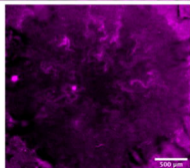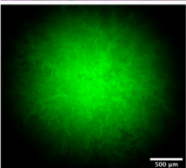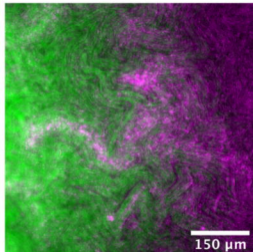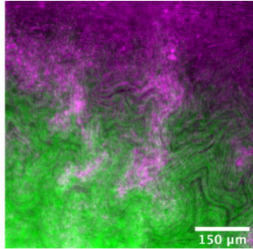611   transport for the intracolony channel system.

a.

85 µm

0 µm

z = 60 µm

500 µm   500 µm

b.

Viable cells
Non-viable cells

500 µm

c.

JM105-miniTn7-gpf
EPS

200 µm

d.

JM105-miniTn7-gpf
Lipid

500 µm

e.

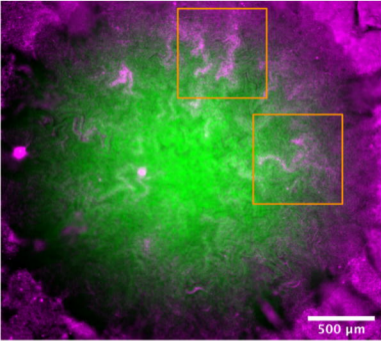JM105-miniTn7-gpf
Protein

60 µm

250 µm

a. Unmixed

500 µm

150 µm

b. Mixed

500 µm

150 µm
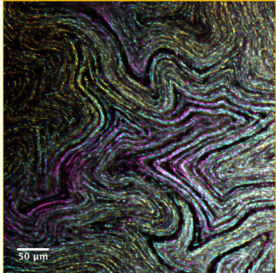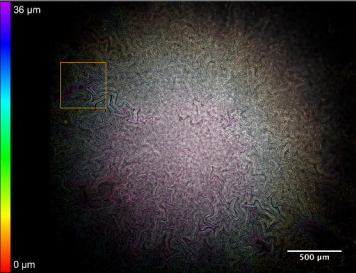
JM105-miniTn7-*gfp*
JM105-miniTn7-*HcRed1*